

# HMT-UNET: A HYBIRD MAMBA-TRANSFORMER VISION UNET FOR MEDICAL IMAGE SEGMENTATION

Mingya Zhang, Limei Gu, Tingshen Ling and Xianping Tao

State Key Laboratory for Novel Software Technology, Nanjing University  
Jiangsu Province Hospital of Chinese Medicine  
dg20330034@smail.nju.edu.cn

## ABSTRACT

In the field of medical image segmentation, models based on both CNN and Transformer have been thoroughly investigated. However, CNNs have limited modeling capabilities for long-range dependencies, making it challenging to exploit the semantic information within images fully. On the other hand, the quadratic computational complexity poses a challenge for Transformers. State Space Models (SSMs), such as Mamba, have been recognized as a promising method. They not only demonstrate superior performance in modeling long-range interactions, but also preserve a linear computational complexity. The hybrid mechanism of SSM (State Space Model) and Transformer, after meticulous design, can enhance its capability for efficient modeling of visual features. Extensive experiments have demonstrated that integrating the self-attention mechanism into the hybrid part behind the layers of Mamba’s architecture can greatly improve the modeling capacity to capture long-range spatial dependencies. In this paper, leveraging the hybrid mechanism of SSM, we propose a U-shape architecture model for medical image segmentation, named Hybird Transformer vision Mamba UNet (HTM-UNet). We conduct comprehensive experiments on the ISIC17, ISIC18, CVC-300, CVC-ClinicDB, Kvasir, CVC-ColonDB, ETIS-Larib PolypDB public datasets and ZD-LCI-GIM private dataset. The results indicate that HTM-UNet exhibits competitive performance in medical image segmentation tasks. Our code is available at <https://github.com/simzhangbest/HMT-UNet>.

**Index Terms**— Medical image segmentation, State Space Models, Transformer, Hybrid model

## 1. INTRODUCTION

As medical imaging technology continues to advance, medical images have become a crucial tool for diagnosing diseases and planning treatments [1]. Among the fundamental and critical techniques in medical image analysis, medical image segmentation holds a significant place. This process involves distinguishing pixels of organs or lesions in medical images,

such as CT scans [2] and Endoscopy [3] videos. Medical image segmentation is one of the most difficult tasks in medical image analysis, with the goal of providing and extracting vital information regarding the shape and volume of these organs or tissues. Deep learning techniques have been used recently to improve medical image segmentation. These models extract useful information from images, increase accuracy, and adapt to different datasets and tasks.

A common approach for semantic image segmentation is the use of an Encoder-Decoder network with skip connections. In this framework, the Encoder captures hierarchical and abstract features from an input image. The Decoder, on the other hand, uses the feature maps produced by the Encoder to build a pixel-wise segmentation mask or map, attributing a class label to each pixel in the input image. Numerous studies have been done to integrate global information into feature maps and enhance multi-scale features, leading to significant enhancements in segmentation performance [4, 5, 6, 7, 8].

Transformers [9] have revolutionized various fields such as computer vision, natural language processing, speech, and robotics, largely due to their adaptive attention mechanism and multimodal adaptability. However, their computational demand grows quadratically with sequence length, posing challenges for training and application.

The innovative State Space Model (SSM) introduced by Mamba [10] offers a solution with its linear time complexity, rivaling or surpassing Transformer performance in language tasks. Mamba’s key innovation lies in its efficient, hardware-conscious selection mechanism for processing lengthy sequences, addressing the scalability issues of traditional Transformers.

Vision Mamba (Vim) [11] employs bidirectional SSMs to overcome Transformer deficiencies in capturing global context and spatial relationships. However, the latency introduced by processing sequences for bidirectional SSMs can complicate training, risk overfitting, and doesn’t guarantee enhanced accuracy. Despite these challenges, ViTs and CNNs often surpass Mamba-based models in visual tasks due to their efficiency and reliability.

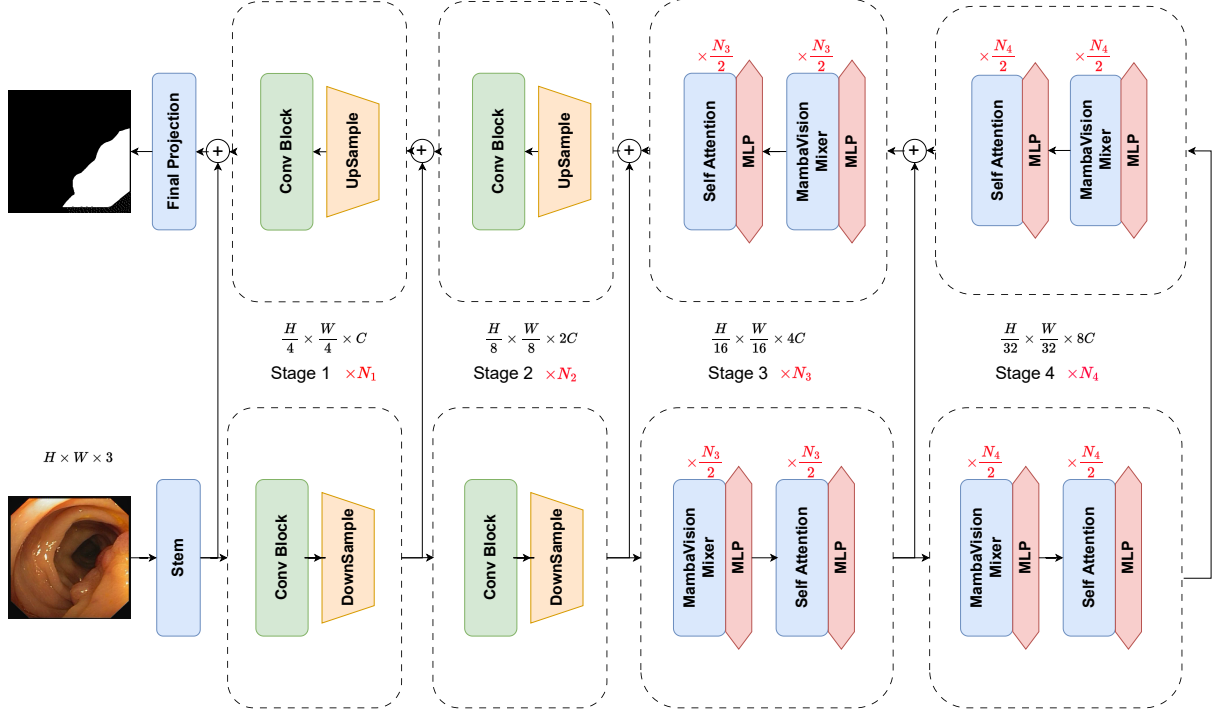


**Fig. 1.** HMT-UNet can be divided into three parts: the encoder, the decoder, and the skip connection. The encoder consists of convolutional modules and Mamba Mixer, The decoder is composed of Mamba Mixer, upsampling operations, convolutional modules, and a final linear layer.

Recently, models that integrate Mamba and Transformer have garnered significant interest among researchers. NVIDIA has introduced MambaVision [12], an innovative hybrid model specifically designed for computer vision tasks, combining the strengths of Mamba and Transformer architectures. It features a hierarchical structure with multi-resolution design, utilizing CNN-based residual blocks to rapidly extract features at various resolutions. Inspired by the success of MambaVision in image classification tasks, this paper introduces for the first time a MambaVision-based UNet model for medical segmentation, the Hybrid Mamba-Transformer Vision UNet (HMT-UNet).

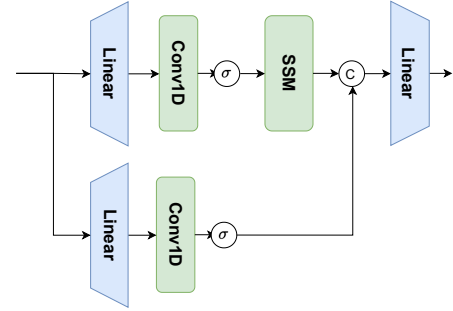


**Fig. 2.** The architecture of MambaVision block.

## 2. METHODS

### 2.1. HMT-UNet Overall Architecture

The main contributions of this paper can be summarized as follows: 1) We propose HMT-UNet, marking the first occasion of exploring the potential applications of purely hybrid models of SSM and Transformer in medical image segmentation. 2) Comprehensive experiments are conducted on public and private datasets, with results indicating that HMT-UNet exhibits considerable competitiveness. 3) We establish a baseline for Hybrid of Mamba and Transformer (HMT) models in medical image segmentation tasks, providing valuable insights that pave the way for the development of more efficient and effective SSM-based segmentation methods.

As shown in Fig 1. HMT-UNet can be divided into three parts: the encoder, the decoder, and the skip connection. The encoder consists of convolutional modules from MambaVision and Mamba Mixer (a hybrid module of VSSM and Transformer), which perform downsampling as the network deepens. The decoder is composed of Mamba Mixer, upsampling operations, convolutional modules, and a final linear layer that serves to restore the dimensions of the segmentation results. For the skip connection, to showcase the segmentation

performance of the purest SSM-based model, we have employed only the simplest addition operation.

The encoder and decoder are structurally symmetric, with the first two layers being CNN-based layers for fast feature extraction at higher input resolutions, and the subsequent two layers being blocks that combine MambaVision and Transformer. Specifically, given an image of size  $H \times W \times 3$ , the input is first converted into overlapping patches with size  $\frac{H}{4} \times \frac{W}{4} \times C$  and projected into a  $C$  dimensional embedding space by the stem which consists of two consecutive  $3 \times 3$  CNN layers with stride of 2. The downsampler in between stages consists of a batch normalized  $3 \times 3$  CNN layer with stride 2 which reduces the image resolution by half. Stage 3 and 4 employ both MambaVision and Transformer blocks. Specifically, given  $N$  layers, we use  $\frac{N}{2}$  MambaVision and MLP blocks which are followed by additional  $\frac{N}{2}$  Transformer and MLP blocks.

In the decoder, each layer in stage 4 and stage 3 must first go through the MambaVision Mixer before being passed to the Transform module. the convolution in stages 2 is also  $3 \times 3$  CNN layer with stride 2 and sample layers, and the Upsample section uses linear upsampling to double the feature size.

## 2.2. Mamba Preliminaries

In contemporary SSM-based models, namely, Structured State Space Sequence Models (S4) and Mamba [10, 13, 14], both depend on a traditional continuous system that maps a one-dimensional input function or sequence, represented as  $x(t) \in R$ , through intermediary implicit states  $h(t) \in R^N$  to an output  $y(t) \in R$ . This process can be depicted as a linear Ordinary Differential Equation (ODE):

$$\begin{aligned} h'(t) &= Ah(t) + Bx(t) \\ y(t) &= Ch(t) \end{aligned} \quad (1)$$

where  $\mathbf{A} \in R^{N \times N}$  represents the state matrix, while  $\mathbf{B} \in R^{N \times 1}$  and  $\mathbf{C} \in R^{N \times 1}$  denote the projection parameters.

The timescale parameter  $\Delta$  and convert  $\mathbf{A}$  and  $\mathbf{B}$  into discrete parameters  $\bar{\mathbf{A}}$  and  $\bar{\mathbf{B}}$  using a consistent discretization rule. The zero-order hold (ZOH) is typically utilized as the discretization rule and can be outlined as follows:

$$\begin{aligned} \bar{\mathbf{A}} &= \exp(\Delta \mathbf{A}) \\ \bar{\mathbf{B}} &= (\Delta \mathbf{A})^{-1}(\exp(\Delta \mathbf{A}) - \mathbf{I}) \cdot \Delta \mathbf{B} \end{aligned} \quad (2)$$

Following discretization, SSM-based models can be calculated in two distinct methods: linear recurrence or global convolution, which are denoted as equations (3) and (4)

$$\begin{aligned} h'(t) &= \bar{\mathbf{A}}h(t) + \bar{\mathbf{B}}x(t) \\ y(t) &= \mathbf{C}h(t) \end{aligned} \quad (3)$$

$$\begin{aligned} \bar{\mathbf{K}} &= (\mathbf{C}\bar{\mathbf{B}}, \mathbf{C}\bar{\mathbf{A}}\bar{\mathbf{B}}, \dots, \mathbf{C}\bar{\mathbf{A}}^{L-1}\bar{\mathbf{B}}) \\ y &= x * \bar{\mathbf{K}} \end{aligned} \quad (4)$$

where  $\bar{\mathbf{K}} \in R^L$  represents a structured convolutional kernel, and  $L$  denotes the length of the input sequence  $x$ .

## 2.3. MambaVision Layer and Mixer

Assuming an input  $X \in \mathbb{R}^{T \times C}$  with sequence length  $T$  with embedding dimension  $C$ , the output of layer  $n$  in stages 3 and 4 can be computed as in

$$\begin{aligned} \hat{X}^n &= \text{Mixer}(\text{Norm}(X^{n-1})) + X^{n-1} \\ X^n &= \text{MLP}(\text{Norm}(\hat{X}^n)) + \hat{X}^n, \end{aligned} \quad (5)$$

Norm and Mixer denote the choices of layer normalization and token mixing blocks, respectively. Without loss of generality, Layer Normalization is used for Norm. Given  $N$  layers, the first  $\frac{N}{2}$  layers employ MambaVision mixer blocks while the remaining  $\frac{N}{2}$  layers employ self-attention.

As shown in Fig. 2, we directly employ the Mamba mixer proposed by MambaVision [12] to perform the Mamba's Vision SSM operations. It is worth noting that the causal convolution in this module has been replaced with regular convolution, as the characteristic of causal convolution, which limits the influence to one direction, is not important in vision tasks. An additional symmetric branch without SSM has been added to the Mixer module, consisting of an additional convolution and SiLU activation, to compensate for any content lost due to the sequential constraints of SSMs. Then, these two branches are concatenated and fed into the final linear layer.

This combination ensures that the final feature representation incorporates both the sequential and spatial information, leveraging the strengths of both branches. We note that the output of each branch is projected into an embedding space with size  $\frac{C}{2}$  (i.e. half the size of original embedding dimension) to maintain similar number of parameters to the original block design. Given an input  $X_{in}$ , the output of MambaVision mixer  $X_{out}$  is computed according to

$$\begin{aligned} X_1 &= \text{Scan}(\sigma(\text{Conv}(\text{Linear}(C, \frac{C}{2})(X_{in})))) \\ X_2 &= \sigma(\text{Conv}(\text{Linear}(C, \frac{C}{2})(X_{in}))) \\ X_{out} &= \text{Linear}(\frac{C}{2}, C)(\text{Concat}(X_1, X_2)), \end{aligned} \quad (6)$$

$\text{Linear}(C_{in}, C_{out})(\cdot)$  denotes a linear layer with  $C_{in}$  and  $C_{out}$  as input and output embedding dimensions, Scan is the selective scan operation as in [10] and  $\sigma$  is the activation function for which Sigmoid Linear Unit (SiLU) [15] is used. In addition, Conv and Concat represent 1D convolution and concatenation operations.

## 2.4. Self-attention

We use a generic multihead self-attention mechanism in accordance to

$$\text{Attention}(Q, K, V) = \text{Softmax}(\frac{QK^T}{\sqrt{d_h}})V. \quad (7)$$

$Q, K, V$  denote query, key and value respectively and  $d_h$  is the number of attention heads. Without loss of generality, the attention formulation which can be computed in a windowed manner similar to previous efforts [16, 17].

### 2.5. Loss function

For our medical image segmentation tasks, we primarily employ basic Cross-Entropy and Dice loss as the loss function cause all of our dataset masks comprise two classes, which are a singular target and the background.

$$\begin{aligned} L_{\text{BceDice}} &= \lambda_1 L_{\text{Bce}} + \lambda_2 L_{\text{Dice}} \\ L_{\text{Bce}} &= -\frac{1}{N} \sum_{i=1}^N [y_i \log(\hat{y}_i) + (1 - y_i) \log(1 - \hat{y}_i)] \\ L_{\text{Dice}} &= 1 - \frac{2|X \cap Y|}{|X| + |Y|} \end{aligned} \quad (8)$$

$(\lambda_1, \lambda_2)$  are constants, with  $(1, 1)$  often selected as the default parameters.

## 3. EXPERIMENTS

### 3.1. Datasets

**Table 1.** In the field of gastroenterology, commonly used publicly available datasets for medical image segmentation are listed in the table, along with their image quantities and sizes.

Dataset	Numbers	Size
Kvasir-SEG	1000	Variable
CVC-ClinicDB	612	$384 \times 288$
Endoscene	912	$574 \times 500$
CVC-ColonDB	380	$574 \times 500$
ETIS	196	$1255 \times 966$
ZD-LCI-GIM	1020	$1280 \times 1024$

**ISIC17 and ISIC18 datasets:** The International Skin Imaging Collaboration 2017 and 2018 challenge datasets (ISIC17 and ISIC18) [18, 19] are two publicly available skin lesion segmentation datasets, containing 2,150 and 2,694 dermoscopy images with segmentation mask labels, respectively.

**Gastrointestinal polyp datasets:** The Kvasir-SEG [20], ClinicDB [21], ColonDB [22], Endoscene [23], and ETIS [24] are currently publicly available polyp datasets, with the number of images and image sizes corresponding to each dataset as shown in Table 1.

**Gastrointestinal GIM dataset:** As shown in Table 1, the ZD-LCI-GIM dataset of gastric intestinal metaplasia, which is an important gastroscopic image data set for observing the possibility of early gastric cancer. This part of the dataset has been proposed by us and will be open-sourced soon.

For these datasets, we provide detailed evaluations on several metrics, including Mean Intersection over Union(mIoU), Dice Similarity Coefficient(DSC), Accuracy(Acc), Sensitivity(Sen), and Specificity(Spe).

### 3.2. Experimental Setup

We adjust the image dimensions in all datasets to  $256 \times 256$  pixels. With the aim of curbing overfitting, we also bring in data augmentation methods, such as random flipping and random rotation. In terms of operational parameters, we have the batch size set at 80, with the AdamW optimizer engaged starting with a learning rate of  $1e-3$ . We make use of CosineAnnealingLR as the scheduler, with its operation spanning a maximum of 50 iterations and the learning rate going as low as  $1e-5$ . We conduct our training over the course of 200 epochs. For the HMT-Unet, the backbone encoder units' weights are initially set to align with those of MambaVision-S. The implementation was carried out on an Ubuntu 20.04 system, using Python 3.9.12, PyTorch 2.0.1, and CUDA 11.7. All experiments are conducted on a single NVIDIA RTX V100 GPU.

### 3.3. Results

We compare HMT-Unet with some state-of-the-art models, presenting the experimental results in Table 2, Table 3, Table 4 and Table 5. For the ISIC and ZD-LCI-GIM datasets, our VM-UNetV2 outperforms other models in terms of the IOU, DSC and Acc metrics. On the Kvasir-SEG, ClinicDB, and ETIS datasets, our algorithm achieved state-of-the-art (SOTA) performance, and it also showed competitive performance on ColonDB and Endoscene.

**Table 2.** Comparative experimental results on the ISIC17 and ISIC18 datasets(Bold indicates the best)

Model	IOU	DSC	Acc	Spe	Sen
UNet [25]	76.98	86.99	95.65	97.43	86.82
UTNetV2 [26]	77.35	87.23	95.84	98.05	84.85
TransFuse [27]	79.21	88.40	96.17	97.98	87.14
MALUNet [28]	78.78	88.13	96.18	98.47	84.78
UNetV2 [29]	82.18	90.22	96.78	98.40	88.71
VM-UNet [14]	80.23	89.03	96.29	97.58	89.90
<b>HMT-Unet</b>	<b>83.05</b>	<b>90.74</b>	<b>96.88</b>	98.02	<b>91.21</b>
UNet [25]	77.86	87.55	94.05	96.69	85.86
UNet++ [5]	78.31	87.83	94.02	95.75	88.65
Att-Unet [30]	78.43	87.91	94.13	96.23	87.60
UTNetV2 [26]	78.97	88.25	94.32	96.48	87.60
SANet [31]	79.52	88.59	94.39	95.97	89.46
TransFuse [27]	80.63	89.27	94.66	95.74	91.28
MALUNet [28]	80.25	89.04	94.62	96.19	89.74
UNetV2 [29]	80.71	89.32	94.86	96.94	88.34
VM-UNet [14]	81.35	89.71	94.91	96.13	91.12
<b>HMT-Unet</b>	<b>81.37</b>	<b>89.73</b>	<b>95.06</b>	<b>97.13</b>	88.64

**Table 3.** Comparative experimental results on the Kvasir-SEG and ClinicDB datasets(Bold indicates the best)

Model	IOU	DSC	Acc	Spe	Sen
UNetV2 [26]	84	91.3	97.47	99.08	88.39
VMUnet [14]	80.32	89.09	96.8	98.49	87.21
VMUnetV2 [32]	84.15	91.34	97.52	99.25	87.71
<b>HMT-Unet</b>	<b>85.66</b>	<b>92.28</b>	<b>97.69</b>	98.7	<b>91.95</b>
UNetV2 [26]	83.85	91.21	98.59	99.16	91.99
VMUnet [14]	81.95	90.08	98.42	99.18	89.73
VMUnetV2 [32]	89.31	94.35	99.09	99.38	<b>95.64</b>
<b>HMT-Unet</b>	<b>90.96</b>	<b>95.26</b>	<b>99.25</b>	<b>99.61</b>	<b>95.05</b>

**Table 4.** Comparative experimental results on the ColonDB, ETIS and Endoscenedatasets(Bold indicates the best)

Model	IOU	DSC	Acc	Spe	Sen
UNetV2 [26]	57.29	72.85	96.19	98.43	68.46
VMUnet [14]	55.28	71.2	96.02	98.45	65.89
VMUnetV2 [32]	<b>60.98</b>	<b>75.76</b>	<b>96.54</b>	<b>98.46</b>	72.68
<b>HMT-Unet</b>	60.44	75.34	96.31	97.97	<b>75.68</b>
UNetV2 [26]	71.9	83.65	98.35	98.61	<b>92.96</b>
VMUnet [14]	66.41	79.81	98.26	99.33	75.79
VMUnetV2 [32]	70.84	82.23	97.43	96.91	91.8
<b>HMT-Unet</b>	<b>71.26</b>	<b>83.22</b>	<b>98.4</b>	<b>98.91</b>	87.59
UNetV2 [26]	<b>82.86</b>	<b>90.63</b>	99.34	99.54	93.82
VMUnet [14]	79.55	88.61	99.2	99.44	92.46
VMUnetV2 [32]	80.32	89.09	99.25	99.55	90.77
<b>HMT-Unet</b>	82.01	90.12	99.29	99.41	<b>95.9</b>

### 3.4. Ablation Study

In this section, we perform ablation studies on the initialization of HMT-UNet, utilizing the ISIC17 and ISIC18 datasets. We initiate HMT-UNet by employing the pre-trained weights obtained from MambaVision-T and MambaVision-S. The findings from our experiments, as depicted in Table 6, demonstrate that the use of more robust pre-trained weights considerably boosts the performance of HMT-UNet in subsequent tasks. This underscores the significant impact that pre-trained weights have on the effectiveness of HMT-UNet.

## 4. CONCLUSION

In this paper, we introduce for the first time a pure MambaVision-based model for medical image segmentation, presenting HMT-UNet as a baseline. To leverage the capabilities of MambaVision-based models, we construct HMT-UNet using MambaVision Mixer layer blocks and initialize its weights with the pretrained MambaVision-S. Comprehensive experiments are conducted on skin lesion and gastroenterology polyp and GIM segmentation datasets indicate that pure

**Table 5.** Comparative experimental results on the ZD-LCI-GIM dataset(Bold indicates the best)

Model	IOU	DSC	Acc	Spe	Sen
DeeplabV3	51.71	68.17	83.71	86.77	73.81
Unet	54.64	70.67	85.61	89.41	73.33
Unet++	55.35	71.26	85.57	88.64	75.65
SwinUnet	54.61	70.64	84.46	86.13	79.08
VM-Unet	56.76	72.42	85.87	88.16	<b>78.48</b>
Unetv2	53.82	69.98	84.63	87.36	75.81
VM-Unetv2	57.02	72.63	86.05	88.46	78.29
<b>HMT-Unet</b>	<b>57.3</b>	<b>72.86</b>	<b>86.61</b>	<b>89.87</b>	76.05

**Table 6.** Ablation studies on Init. Weight of MambaVision

Init. Weight	ISIC17		ISIC18	
	IOU	DSC	IOU	DSC
-	69.63	82.1	73.13	84.6
MambaVision-T	78.85	88.17	79.04	88.29
MambaVision-S	83.05	90.74	81.37	89.73

MambaVision-based models are highly competitive in medical image segmentation tasks and merit in-depth exploration in the future.

## 5. REFERENCES

- [1] Jie-Zhi Cheng, Dong Ni, Yi-Hong Chou, Jing Qin, Chui-Mei Tiu, Yeun-Chung Chang, Chiun-Sheng Huang, Dinggang Shen, and Chung-Ming Chen, “Computer-aided diagnosis with deep learning architecture: applications to breast lesions in us images and pulmonary nodules in ct scans,” *Scientific reports*, vol. 6, no. 1, pp. 24454, 2016.
- [2] Rotem Golan, Christian Jacob, and Jörg Denzinger, “Lung nodule detection in ct images using deep convolutional neural networks,” in *2016 international joint conference on neural networks (IJCNN)*. IEEE, 2016, pp. 243–250.
- [3] Dehua Tang, Lei Wang, Tingsheng Ling, Ying Lv, Muhan Ni, Qiang Zhan, Yiwei Fu, Duanming Zhuang, Huimin Guo, Xiaotan Dou, et al., “Development and validation of a real-time artificial intelligence-assisted system for detecting early gastric cancer: A multicentre retrospective diagnostic study,” *EBioMedicine*, vol. 62, 2020.
- [4] Jieneng Chen, Yongyi Lu, Qihang Yu, Xiangde Luo, Ehsan Adeli, Yan Wang, Le Lu, Alan L Yuille, and Yuyin Zhou, “Transunet: Transformers make strong encoders for medical image segmentation,” *arXiv preprint arXiv:2102.04306*, 2021.

- [5] Zongwei Zhou, Md Mahfuzur Rahman Siddiquee, Nima Tajbakhsh, and Jianming Liang, "Unet++: A nested unet architecture for medical image segmentation," in *Deep Learning in Medical Image Analysis and Multimodal Learning for Clinical Decision Support: 4th International Workshop, DLMIA 2018, and 8th International Workshop, ML-CDS 2018, Held in Conjunction with MICCAI 2018, Granada, Spain, September 20, 2018, Proceedings 4*. Springer, 2018, pp. 3–11.
- [6] Shu Liu, Lu Qi, Haifang Qin, Jianping Shi, and Jiaya Jia, "Path aggregation network for instance segmentation," in *Proceedings of the IEEE conference on computer vision and pattern recognition*, 2018, pp. 8759–8768.
- [7] Liang-Chieh Chen, Yukun Zhu, George Papandreou, Florian Schroff, and Hartwig Adam, "Encoder-decoder with atrous separable convolution for semantic image segmentation," in *Proceedings of the European conference on computer vision (ECCV)*, 2018, pp. 801–818.
- [8] Sanghyun Woo, Jongchan Park, Joon-Young Lee, and In So Kweon, "Cbam: Convolutional block attention module," in *Proceedings of the European conference on computer vision (ECCV)*, 2018, pp. 3–19.
- [9] Ashish Vaswani, Noam Shazeer, Niki Parmar, Jakob Uszkoreit, Llion Jones, Aidan N. Gomez, Łukasz Kaiser, and Illia Polosukhin, "Attention is all you need," in *Advances in Neural Information Processing Systems*, 2017, pp. 5998–6008.
- [10] Albert Gu and Tri Dao, "Mamba: Linear-time sequence modeling with selective state spaces," *arXiv preprint arXiv:2312.00752*, 2023.
- [11] Lianghui Zhu, Bencheng Liao, Qian Zhang, Xinlong Wang, Wenyu Liu, and Xinggang Wang, "Vision mamba: Efficient visual representation learning with bidirectional state space model," *arXiv preprint arXiv:2401.09417*, 2024.
- [12] Ali Hatamizadeh and Jan Kautz, "Mambavision: A hybrid mamba-transformer vision backbone," *arXiv preprint arXiv:2407.08083*, 2024.
- [13] Yue Liu, Yunjie Tian, Yuzhong Zhao, Hongtian Yu, Lingxi Xie, Yaowei Wang, Qixiang Ye, and Yunfan Liu, "Vmamba: Visual state space model," *arXiv preprint arXiv:2401.10166*, 2024.
- [14] Jiacheng Ruan and Suncheng Xiang, "Vm-unet: Vision mamba unet for medical image segmentation," *arXiv preprint arXiv:2402.02491*, 2024.
- [15] Stefan Elfving, Eiji Uchibe, and Kenji Doya, "Sigmoid-weighted linear units for neural network function approximation in reinforcement learning," *Neural Networks*, vol. 107, pp. 3–11, 2018.
- [16] Ze Liu, Yutong Lin, Yue Cao, Han Hu, Yixuan Wei, Zheng Zhang, Stephen Lin, and Baining Guo, "Swin transformer: Hierarchical vision transformer using shifted windows," in *Proceedings of the IEEE/CVF International Conference on Computer Vision*, 2021, pp. 10012–10022.
- [17] Ze Liu, Han Hu, Yutong Lin, Zhuliang Yao, Zhenda Xie, Yixuan Wei, Jia Ning, Yue Cao, Zheng Zhang, Li Dong, and et al., "Swin transformer v2: Scaling up capacity and resolution," in *Proceedings of the IEEE/CVF Conference on Computer Vision and Pattern Recognition*, 2022, pp. 12009–12019.
- [18] Matt Berseth, "Isic 2017-skin lesion analysis towards melanoma detection," *arXiv preprint arXiv:1703.00523*, 2017.
- [19] Noel Codella, Veronica Rotemberg, Philipp Tschandl, M Emre Celebi, Stephen Dusza, David Gutman, Brian Helba, Aadi Kalloo, Konstantinos Liopyris, Michael Marchetti, et al., "Skin lesion analysis toward melanoma detection 2018: A challenge hosted by the international skin imaging collaboration (isic)," *arXiv preprint arXiv:1902.03368*, 2019.
- [20] Debesh Jha, Pia H Smedsrud, Michael A Riegler, Pål Halvorsen, Thomas de Lange, Dag Johansen, and Håvard D Johansen, "Kvasir-seg: A segmented polyp dataset," in *MultiMedia Modeling: 26th International Conference, MMM 2020, Daejeon, South Korea, January 5–8, 2020, Proceedings, Part II 26*, 2020, pp. 451–462.
- [21] Jorge Bernal, F Javier Sánchez, Gloria Fernández-Esparrach, Debora Gil, Cristina Rodríguez, and Fernando Vilariño, "Wm-dova maps for accurate polyp highlighting in colonoscopy: Validation vs. saliency maps from physicians," *Computerized medical imaging and graphics*, vol. 43, pp. 99–111, 2015.
- [22] Nima Tajbakhsh, Suryakanth R Gurudu, and Jianming Liang, "Automated polyp detection in colonoscopy videos using shape and context information," *IEEE transactions on medical imaging*, vol. 35, no. 2, pp. 630–644, 2015.
- [23] David Vázquez, Jorge Bernal, F Javier Sánchez, Gloria Fernández-Esparrach, Antonio M López, Adriana Romero, Michal Drozdal, and Aaron Courville, "A benchmark for endoluminal scene segmentation of colonoscopy images," *Journal of healthcare engineering*, vol. 2017, no. 1, pp. 4037190, 2017.
- [24] Juan Silva, Aymeric Histace, Olivier Romain, Xavier Dray, and Bertrand Granado, "Toward embedded detection of polyps in wce images for early diagnosis of col-

orectal cancer,” *International journal of computer assisted radiology and surgery*, vol. 9, pp. 283–293, 2014.

- [25] Olaf Ronneberger, Philipp Fischer, and Thomas Brox, “U-net: Convolutional networks for biomedical image segmentation,” in *Medical Image Computing and Computer-Assisted Intervention–MICCAI 2015: 18th International Conference, Munich, Germany, October 5–9, 2015, Proceedings, Part III* 18. Springer, 2015, pp. 234–241.
- [26] Yunhe Gao, Mu Zhou, D Liu, and D Metaxas, “A multi-scale transformer for medical image segmentation: Architectures, model efficiency, and benchmarks,” *arXiv preprint arXiv:2203.00131*, 2022.
- [27] Yundong Zhang, Huiye Liu, and Qiang Hu, “Transfuse: Fusing transformers and cnns for medical image segmentation,” in *Medical Image Computing and Computer Assisted Intervention–MICCAI 2021: 24th International Conference, Strasbourg, France, September 27–October 1, 2021, Proceedings, Part I* 24. Springer, 2021, pp. 14–24.
- [28] Jiacheng Ruan, Suncheng Xiang, Mingye Xie, Ting Liu, and Yuzhuo Fu, “Malunet: A multi-attention and light-weight unet for skin lesion segmentation,” in *2022 IEEE International Conference on Bioinformatics and Biomedicine (BIBM)*. IEEE, 2022, pp. 1150–1156.
- [29] Yaopeng Peng, Milan Sonka, and Danny Z Chen, “U-net v2: Rethinking the skip connections of u-net for medical image segmentation,” *arXiv preprint arXiv:2311.17791*, 2023.
- [30] Ozan Oktay, Jo Schlemper, Loic Le Folgoc, Matthew Lee, Mattias Heinrich, Kazunari Misawa, Kensaku Mori, Steven McDonagh, Nils Y Hammerla, Bernhard Kainz, et al., “Attention u-net: Learning where to look for the pancreas,” *arXiv preprint arXiv:1804.03999*, 2018.
- [31] Jun Wei, Yiwen Hu, Ruimao Zhang, Zhen Li, S Kevin Zhou, and Shuguang Cui, “Shallow attention network for polyp segmentation,” in *Medical Image Computing and Computer Assisted Intervention–MICCAI 2021: 24th International Conference, Strasbourg, France, September 27–October 1, 2021, Proceedings, Part I* 24. Springer, 2021, pp. 699–708.
- [32] Mingya Zhang, Yue Yu, Sun Jin, Limei Gu, Tingsheng Ling, and Xianping Tao, “Vm-unet-v2: Rethinking vision mamba unet for medical image segmentation,” in *International Symposium on Bioinformatics Research and Applications*. Springer, 2024, pp. 335–346.